ACS OMEGA

http://pubs.acs.org/journal/acsodf

Article

Improvement in Slurry Erosion and Corrosion Resistance of Plasma-Sprayed Fly Ash Coatings for Marine Applications

Nagarjuna Chavana, Vishwanath Bhajantri F, and Sudhakar C. Jambagi*

Cite This: *ACS Omega* 2022, 7, 32369−32382

Read Online

ACCESS | Metrics & More | Article Recommendations

ABSTRACT: Fly ash (FA), a multicompound mineral, is an industrial waste produced during coal burning in thermal power stations. It has been regarded as the most environmentally hazardous material. Furthermore, handling FA has been a significant challenge for many developing countries. Therefore, researchers have been exhorted to enhance its usage to counter its handling issues. FA is enriched with mullite, silica, and alumina. Having such mineralogy, FA can be envisaged as a promising candidate for combating erosion and corrosion in marine environments. With this motivation, the research aims to deposit as-received FA using the plasma-spraying technique onto a marine-grade steel substrate without additives and assess the performance of such coatings for erosion and corrosion properties. The coating has exhibited more than 100% improvement in microhardness. The erosion resistance was improved by ∼11% compared to that of the uncoated sample, which is attributed to the hardness to elastic modulus ratio (H/E) and its unique mineralogy. The minor improvement in erosion resistance was attributed to the coating's poor fracture toughness. The erosion study shows that slurry concentration and rotational speeds were the most influential parameters. The scar depth was significantly shallower for FA-coated samples. The corrosion resistance has improved only by ∼13.49%, owing to the porous nature of the coating. Therefore, such coatings with appropriate improvements in their properties are expected to assuage both environmental and industrial challenges.

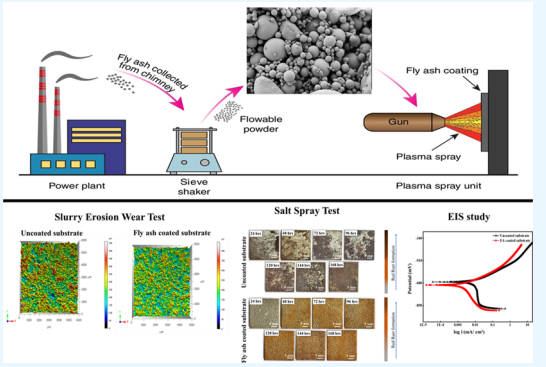

INTRODUCTION

Fly ash (FA) is a solid waste byproduct produced in thermal power stations by burning coal, oil, and biofuels. According to the Central Electrical Authority of India report (August 2021−22), the total generation of FA has been ∼232.56 MT from burning ∼686.34 MT of coal.[1] The large amounts of FA generated require large areas of landfill; thus, FA disposal causes severe environmental fallouts—soil degradation, air pollution, groundwater contamination, hindered crop growth, and human health hazards.[2] Handling FA has been a growing global concern for developing countries. Hence, governments in respective countries have taken active initiatives to improve FA utilization. Consequently, researchers have even started exploring various avenues to tap FA's potential in agriculture, brick manufacturing,[3−5] glass ceramics, glass materials,[6] and engineering applications[7,8] among others extensively used in cement and construction domains.[9−11] Few studies have focused on converting FA into zeolites.[12−16] Zeolites are minerals of aluminum and silicon compounds employed in sorption, catalysis, and ion exchange, and have a range of benefits as a replacement in producing ecologically acceptable goods.[17] FA predominantly consists of spherical solid and hollow spheres (cenospheres) with unburned carbonaceous matter.[15] Cenospheres have found applications in various naval and automobile components as reinforcement materials.[18] Nevertheless, these cenospheres are only a tiny, hollow, and small fraction of as-received FA.[19] However, preprocessing techniques of FA to produce cenospheres will be expensive and limit the fullest extent of the utility of FA. FA contains oxides such as SiO_2, Al_2O_3, CaO, and Fe_2O_3. According to ASTM C-618,[20] FA is categorized into two groups based on its chemical composition: class F (made from anthracite and bituminous coals) and class C (usually produced from lignite and sub-bituminous coals). These chemical variants are differentiated based on the ash's traces of calcium, silica, alumina, and iron oxides. Class F series FA contains 70% or more (by mass) silicon, aluminum, and iron oxides, whereas for class C, this percentage lies between 50% and 70%.[20] The above classification was also based on the weight fraction of CaO. Since as-received FA is a multicompound mineral, it has

Received: June 18, 2022
Accepted: August 17, 2022
Published: September 1, 2022

excellent potential in thermal spray coatings.[21] Therefore, the current work aims to understand the full potential of as-received FA, involving complex compounds, such as mullite, for potential use in marine applications.

Plasma spraying is a thermal spraying process in which an arc is struck between electrodes and noble gases are fed in the vicinity for ionization, forming a plasma plume to melt and accelerate powder particles onto a substrate surface.[22] Upon impact, these molten particles cool and solidify quickly by transmitting heat to the underlying substrate, forming a lamellae-like coating. Such layer-by-layer deposition can build a coating of desired thickness. Plasma spraying is a versatile thermal spray process for ceramic powders that protects technical components against wear, heat, or corrosion.[23] So far, corrosion studies of plasma-sprayed ceramic and cermet powders showed corrosion resistance that was greatly influenced by the coatings' porosity, thickness, surface roughness, and the corrosion medium.[24,25] However, these aspects were not explored in detail.

Few researchers have used FA alone as a feedstock material for the deposition of coatings. Rama Krishna et al.[26] were the first to study the viability of using FA alone using a detonation gun. The FA coatings' microhardness was improved because of its alumina-rich mineralogy. Another study by Sidhu et al.[27] investigated the wear, oxidation, and salt corrosion behavior of plasma-sprayed FA coating. As expected, the FA coating outperformed carbon steel substrates in oxidation and salt corrosion resistance even at 900 °C because of the silica and alumina phases. Muhammad et al.[28] have studied the effect of plasma spray process parameters on the properties of FA coatings on marine-grade steel; they reported a higher hardness (500 $HV_{0.1}$) for coatings of thicknesses less than 200 μm. Further, Kılıçay's group used the plasma transferred arc (PTA) method to enhance the microstructural properties and wear resistance of plasma-sprayed aluminum oxide, chromium oxide, WC-Co, and Cr_3C_2−NiCr powders onto a 90MnCrV8 steel surface.[29,30] Some researchers have used fly ash with additives as a feedstock material for plasma spray coating. Naveena et al.[31] investigated the individual effect of slurry erosion process parameters on erosive wear behavior of plasma-sprayed FA−50% alumina coatings on Al6061 substrate. The coated samples showed an improvement in slurry erosive resistance and slurry rotational speed, and slurry concentrations were more influential than the slurry particle size. The same research group studied the corrosion behavior of plasma-sprayed FA−50% SiC and FA−50% Al_2O_3 composite coatings on Al-6061.[32] It was found that FA−50% SiC composite coatings showed better corrosion resistance than FA−50% Al_2O_3 coating and uncoated substrate for the test duration of 48 h. The poor corrosion resistance of the FA−50% Al_2O_3 coating was attributed to the formation of γ-alumina during the coating deposition. However, the researchers in this domain did not provide greater insight into the combined effect of process parameters and the impact of the as-received FA coating's mechanical properties on the performance of slurry erosive wear. Also, the limited test duration of the corrosion test fails to determine the stable corrosion rate of the coatings. Moreover, reports concerning pristine FA are scanty.

In this work, the experimental investigation of the slurry erosion test, varying processing parameters/independent variables, was conducted using the design of experiments (DOE) using the full factorial design (FFD) method. This approach allows the researcher to perform the experiments and determine cause-and-effect relationships with a minimal number of experiments. The FFD provides the optimum experimental design to make sufficient data available for analysis. The experiments were designed for three processing parameters: sand particle size, slurry concentration, and rotational speed. The effect of the processing parameters on output response parameters was studied. Statistical analysis of the responses was carried out using ANOVA (analysis of variance).

To date, FA alone has never been explored to the fullest extent as a coating despite its high hardness, erosion, and corrosion resistance. The current work investigates the properties of FA coating deposited using plasma spray on a marine-grade steel substrate. The coatings' mechanical properties, slurry erosion, and corrosion resistance (salt spray) were studied. The electrochemical impedance spectroscopy technique was used to affirm the corrosion study. At every stage, the coated sample performance was compared with that of uncoated samples. This work's primary focus is to highlight fly ash usage in the surface engineering domain to meet various industrial applications.

MATERIALS AND METHODS

Powder Preparation. This work used as-received FA powder as a feedstock material for coating. FA was collected from Raichur Thermal Power Station, Raichur, Karnataka. In the as-received FA, the particle size ranges from 2 to 180 μm. The particle size selection of the feedstock powder is crucial as it influences the flowability.[33,34] Flowability improves with a narrow particle size distribution, as small and finer particles often cause inconsistent flow because of interparticle friction. So, the as-received FA was mechanically sieved in the range of 106−125 μm particle size to enhance flowability.

Substrate Material and Coating Deposition. The substrate was marine-grade steel (IS2062 grade B). Before coating, substrates were ultrasonically cleaned using isopropyl alcohol, followed by grit blasting. Then, the sieved FA powders were deposited onto the substrate using the atmospheric plasma spraying (APS) technique using a plasma spray gun (MEC, 9MBM, India). The details of the operating plasma spray parameters are listed in Table 1.

Characterization of Powder and Coating Techniques. A field emission scanning electron microscope (FESEM) (Carl Zeiss, Supra-300, Germany) was used for the morphological study of powders and FA-coated and tested samples. The coated samples were sliced into pieces using a diamond saw

Table 1. Operating Parameters for the Plasma Spraying Technique (MEC, Jodhpur)

operating parameters	values
primary gas (Ar) flow rate (SLPM)	40
secondary gas (H_2) flow rate (SLPM)	5
current (A)	600
voltage (V)	65
carrier gas (Ar) flow rate	4
powder feed rate (g/min)	20
stand-off distance (mm)	75
nozzle diameter (mm)	6
powder injector (mm)	2
powder injector angle (deg)	90

https://doi.org/10.1021/acsomega.2c03800
ACS Omega 2022, 7, 32369−32382

and fine-polished according to ASTM G1-03[35] to access the microstructure and porosity of the coatings. An X-ray diffractometer (XRD) (Malvern PANalytical, Empyrean, United Kingdom) was used for phase identification of the sieved FA powders and as-sprayed FA coatings. The XRD was operated using Cu Kα radiation (λ = 1.542 Å) with a current of 20 mA, an accelerating voltage of 30 kV, and the scanning rate of 1° min^{-1} in the 2θ range of 10−90°. Further, wavelength-dispersive X-ray fluorescence (WD-XRF) (Malvern PANalytical, Zetium, United Kingdom) was used to quantify the chemical composition of the sieved FA. The coating thickness was evaluated by taking an average of 10 measurements along with the cross-sectional image of the coating, and porosity was determined by Image analysis.

Mechanical Properties of the Coating. Coating adhesion strength was evaluated using the coating pull-out method according to ASTM C 633-13.[36] The cross sections of coated and counterpart samples were initially glued using HTK Ultra Bond epoxy resin, and the samples were cured for 24 h at room temperature. Under ambient circumstances, the test was performed on a universal tensile machine (Shimadzu hydraulic tensile machine, AG-X Plus, Japan) with a strain rate of 0.016 m/s to assess bond strength. The test was repeated five times to get the standard deviation value of the maximum normal load that the glued samples could withstand. The adhesion strength was then calculated using eq 1:

$$\text{adhesion strength} = P/A \tag{1}$$

where P is the maximum applied average normal load in newtons, A is the glued cross-sectional area of the sample in square millimeters, and adhesion strength is in megapascals.

The microhardness was measured using a Vickers microhardness tester (Mitutoyo, HM-200, Japan) with an indentation load of 300 g and a dwell period of 15 s. Indentions were made on a polished cross-sectional surface from the substrate to the coating across the interface. Five indentations were made at each region, and the average values were noted.

The elastic modulus was determined using depth-sensing indentations. The indentations were made using a Berkovich indenter attached to an instrumented hardness tester (KLA, Nano Indenter G200, U.S.A.) at the cross section of the coating and substrate. The depth and area function correlation was established by calibrating the indenter with a standard fused quartz sample. Each indentation test consists of loading, dwelling (keeping the indent at peak load), and unloading conditions. During the loading cycle, the maximum load of 50 mN was reached in 10 s, sustained for 10 s, and removed in 10 s. Five indentations were made at various points along the cross section of the coating and substrate, and the average value was noted. The elastic modulus was calculated using the Oliver−Pharr method.[37] The equation for reduced elastic modulus (E_r) is given by

$$\frac{1}{E_r} = \frac{1-\nu_c^2}{E_c} + \frac{1-\nu_i^2}{E_i} \tag{2}$$

where ν_i, E_i, ν_c, and E_c are the Poisson's ratio and elastic modulus of the indenter and coating, respectively. The reduced modulus was also calculated using eq 3:

$$E_r = 0.15\left(\frac{\pi}{A}\right)^{0.5}\left(\frac{dP}{dH}\right) \tag{3}$$

where dP/dH is the slope of the unloading curve's upper part in the load−depth plot; π is a constant. The elastic modulus of the coating and substrate was evaluated using eqs 2 and 3.

The fracture toughness was evaluated using the indentation method. Three indentations were made at the cross section of the coating by a microhardness indenter (Mitutoyo, HM-200, Japan) to develop cracks, as shown in Figure 1. The crack

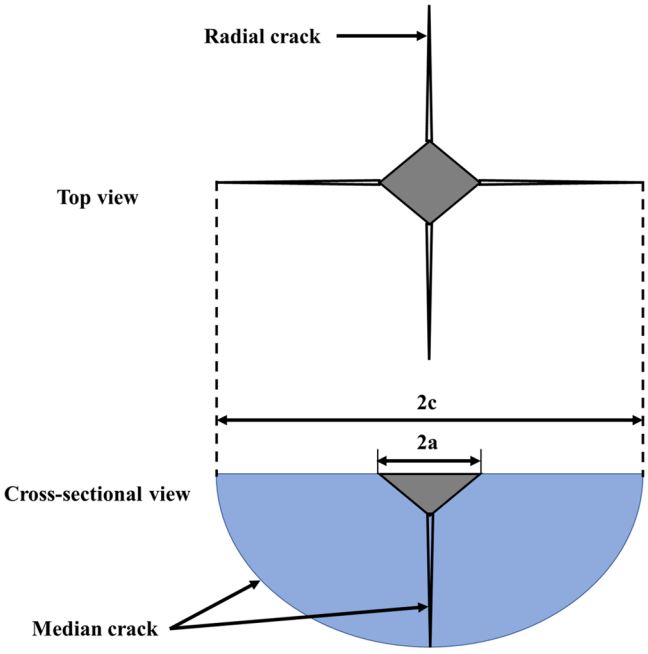

Figure 1. Schematic of crack formation by Vickers indentation.

lengths were measured using ImageJ software, and the mean crack length was considered for computing the fracture toughness (K_{Ic}) using the Anstis equation, median crack model:[38]

$$K_{Ic} = 0.016\left(\frac{P}{C^{1.5}}\right)\left(\frac{E}{H_v}\right)^{0.5} \tag{4}$$

where P is the normal load applied in newtons, C is the average half-crack length from the center of the indentation, E is the elastic modulus, and H_v is the microhardness of the coating.

The spacing between all the indentations made for evaluating microhardness, elastic modulus, and crack generation must be at least 3 times bigger than the diagonal of the highest indentation to avoid the influence of stress fields around indentations.[39]

Slurry Erosion Test. Slurry erosive wear tests were carried out on uncoated FA coatings of 25 × 25 × 10 mm^3 using a slurry erosion test rig (Novus Tribosolutions, SEW-P06, Bangalore). Before testing, the samples were cleaned using isopropyl alcohol, and initial weights were measured using an electronic digital microbalance (Contech Instruments Ltd., CAI-234, India) with 0.01 mg accuracy. The slurry erosion test apparatus consists of six spindles whose speed was regulated using an electric motor. The samples were fixed on the spindles with the help of a nut and bolt system. All the pieces were immersed in slurry cups made of stainless steel. A motor-driven vertical spindle supports the round-shaped specimen holder that holds the coated and uncoated specimens at equal spacing. The slurry cups are closed with a rubber seal to avoid slurry

https://doi.org/10.1021/acsomega.2c03800
ACS Omega 2022, 7, 32369−32382

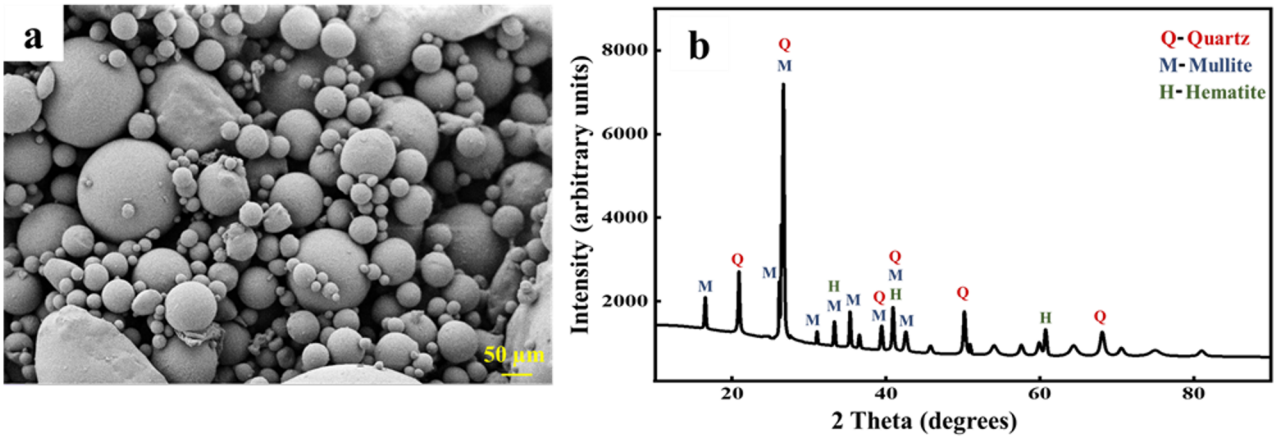

Figure 2. (a) Morphology of FA particles and (b) XRD pattern of the FA powder.

Table 2. Chemical Composition of FA

compd	SiO_2	Al_2O_3	CaO	Fe_2O_3	MgO	K_2O	Na_2O	TiO_2	P_2O_5	LOI
wt %	70.57	09.63	06.49	05.84	02.05	02.56	01.03	0.93	0.30	0.60

leakage. The slurry was prepared by mixing different proportions of silica sand in a 3.5% NaCl solution. Studies were carried out at different sand concentrations (100, 200, and 300 g/L), varying spindle speeds (500, 1000, and 1500 rpm), and different sand particle sizes (200, 312, and 425 μm). A standard experimental plan was established using three-level FFD, as shown in Table 4. All the tests were repeated three times, and the average weight loss values were noted. The tested samples were dried and cleaned with isopropyl alcohol, and then the weight loss was measured using a digital electronic microbalance. After the test, eroded surfaces were analyzed using FESEM and a 3D profilometer (NANOVEA, ST400, U.S.A.). The average volume loss and depth profiles of the tested samples were quantified by considering five different locations on the eroded surface.

Design of Experiments and Analysis of Variance. The impact of various parameters such as sand particle size, slurry rotational speed, and slurry concentration for uncoated and FA-coated marine-grade steel was analyzed using DOE with a three-level FFD containing 27 experiments. The total number of experiments (N_{exp}) was calculated using eq 5. The values of the parameters were coded and varied over three levels, as shown in Table 4.

$$N_{exp} = a^k \tag{5}$$

where N_{exp} is the total number of experiments, k is the number of processing parameters/independent factors, and a is the number of levels for each parameter.

The statistical tool "Minitab 2021" was used for the experimental design and the analysis (statistical and graphical) of the experimental result. The significance of each parameter to weight loss was calculated using the ANOVA responses of FA-coated and uncoated samples. The significance of each parameter in the model was analyzed by computing the P-value.

Corrosion Study. *Salt Spray Test.* The salt spray test was conducted for uncoated and FA-coated marine-grade steel samples in a salt spray apparatus (Culture Instruments, NSS01, Bangalore). Initial weights of the samples were measured using an electronic digital weighing balance with 0.01 mg accuracy after cleaning with isopropyl alcohol. The samples were placed in a salt chamber where a solution of 3.5% NaCl and compressed air was sprayed at constant pressure and temperature. The test was conducted for 168 h, and for every 24 h, a variation in weight loss was recorded. The experiment was conducted by the instructions laid down in ASTM B117-18 standards.[40] The pH of the salt bath was kept at 7.08, and the temperature was 35 ± 2 °C. After the salt-spraying test, the specimens were cleaned with isopropyl alcohol and compressed air to eliminate corroded products. The final weights of the samples were computed, and then the corrosion rate was assessed using ASTM G31-72.[41]

Electrochemical Impedance Spectroscopy (EIS) Test. The corrosion behavior was evaluated using an electrochemical corrosion analyzer (ACM instruments, ACM Gill AC-1684, United Kingdom) for FA-coated and uncoated marine-grade steel samples in 3.5% NaCl solution. The samples were metallurgically polished before the test using different polishing cloths to achieve a good surface finish. After attaining a mirror-like surface finish, the samples were placed in a corrosion kit where a 1 cm^2 area of the sample was exposed to the testing media. All the tests were conducted at a temperature of 25 °C.

RESULTS AND DISCUSSION

Characterization of the Powders and Coatings. An FESEM image of sieved FA powder is shown in Figure 2a. The sieved FA contains solid spheres of different particle sizes, and the particles did not decompose during preprocessing. Figure 2b depicts the XRD patterns of sieved FA, and it contains quartz (COD no. 96-901-2601), mullite (COD no. 96-900-1568), and hematite (COD no. 96-101-1268) peaks at 2θ angles of 26.64°, 26.30°, and 33.14°, respectively. Further, the percentage occupancy of each phase was determined by WD-XRF on the sieved FA particles. The occupancies of SiO_2, Al_2O_3, CaO, and Fe_2O_3 were 70.57%, 9.63%, 6.49%, and 5.84%, respectively. Apart from these, the other phases showed minor occupancies, as in Table 2. From the WD-XRF, it is evident that silica and alumina are the major constituents in FA. This lean mixture of alumina is mixed with silica and forms a complex structure like mullite, as shown in the XRD. Since

https://doi.org/10.1021/acsomega.2c03800
ACS Omega 2022, 7, 32369−32382

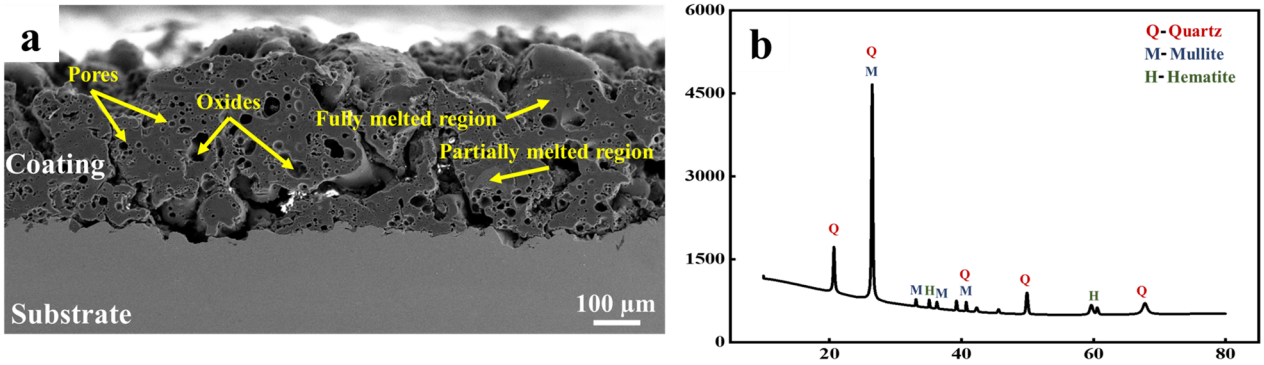

Figure 3. (a) Microstructure of the FA coating and (b) XRD pattern of the FA coating.

the fraction of Si, Al, and Fe oxides occupancy is more than 70%, the FA used in the current study is categorized as class F, according to ASTM C-618.[20]

Figure 3a shows the microstructure of a well-adhered FA coating on the substrate without any crack at the interface. The coating thickness was ~291.72 ± 26.89 μm with a 16−18% porosity for a powder particle size ranging from 106 to 125 μm. The higher porosity of the coating was attributed to large-sized FA particles.[28] These particles were porous with a high specific surface area and low specific gravity. Such particles are expected to interact less with the plasma flame, forming partially melted regions within the coating. Sidhu et al.[27] reported 5−7% porosity for a particle size ranging from 63 to 120 μm for plasma-sprayed coatings. However, the flowability of FA powders will be a significant challenge for a broader particle size distribution.[42]

The microstructure of FA coatings exhibits bimodality, i.e., partially and fully molten regions. Such microstructures typically form because of the significant size variation in the powder particles. Coarser or large particles partially melt at lower temperatures owing to their high mass and volume. In contrast, the finer particles produce fully melted regions which is due to a higher degree of melting.[43,44] Bimodal microstructures significantly influence the mechanical properties with their lower porosity and better interlamellar interactions.[22] Moreover, the mechanical properties of the FA coating could even be improved with higher porosity owing to its rich mineral sources, namely, quartz and mullite. Further improvement in the properties could be achieved by adding alumina and carbon nanotubes (CNT).

Figure 3b illustrates the phase composition of FA coatings. The coatings could successfully retain all the significant phases available at the powder stage. The quartz (COD no. 96-900-5021) and mullite (COD no. 96-900-1322) appeared at 2θ angles of 26.53° and 26.17°, respectively. Mullite is a stable intermediate phase of an alumina-rich silica compound; it finds applications in advanced structures because of its high melting point, low coefficient of thermal expansion, excellent creep resistance, high strength, and good chemical stability.[45,46] Also, mullite has high deformation resistance, enhancing the hardness and other mechanical properties.[47,48]

Mechanical Properties of the Coating. Adhesion strength is among the essential parameters in coating performance and durability. Good adhesion strength is a pivotal property for wear-resistant coatings. The tendency of a coating to adhere to the substrate during coating performance is defined as adhesion strength. If the fracture occurs at the coating−substrate interface, it is called adhesion failure. If the rupture occurs within the coating, it is regarded as a failure due to its cohesion.[22,49] By knowing the load corresponding to failure (~2.76 ± 0.11 kN), the adhesion strength (~5.62 ± 0.23 MPa) was calculated using eq 1. The plasma spray technique achieves bonding solely because of mechanical interlocking. Because of the impact pressure, the imperfections of a rough surface were filled by spreading molten materials, and subsequent solidification led to mechanical interlocking.[22] From Figure 4a, it is evident that the coating failure due to

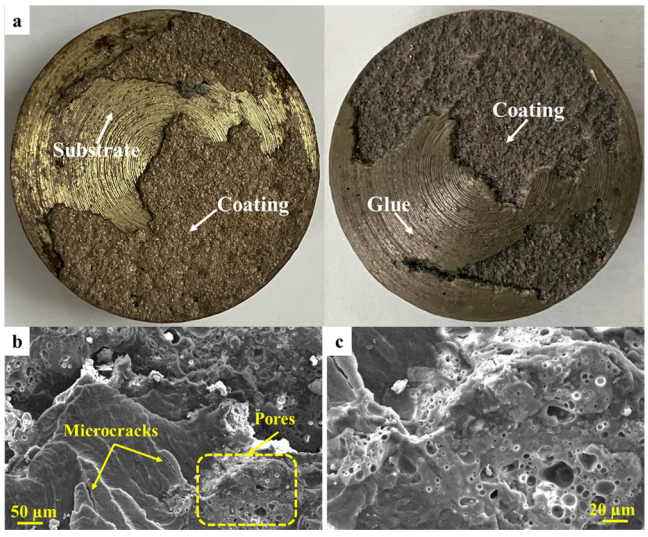

Figure 4. Surface morphology of the samples after the pull-out test: (a) photographs and (b and c) FESEM images at lower and higher magnification, respectively.

both cohesion and adhesion modes occurred. Parts b and c of Figure 4 show that the coating failed because of interlamellar cracks and micropores. Yilmaz[50] reported higher adhesion strength (~28.56 MPa) for Al_2O_3−13 wt % TiO_2 with a bond coat than Al_2O_3−13 wt % TiO_2 without a bond coat (~7.95 MPa). Therefore, the adhesion strength of the FA coating can be improved by using a bond coat and using additives, such as alumina, to the as-received FA. Such studies are underway and will be communicated in the future.

The microhardness of the substrate, the substrate−coating interface, and the top coat are shown in Figure 5. The microhardness of the FA coating was observed to have an ~108.67% improvement compared to that of the substrate; it can be ascribed to the presence of a hard mullite phase in the FA coating. Likewise, the microhardness at the interface was

https://doi.org/10.1021/acsomega.2c03800
ACS Omega 2022, 7, 32369−32382

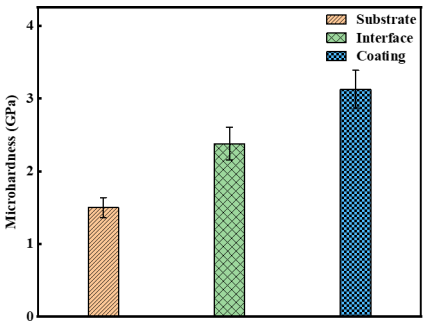

Figure 5. Microhardness of the sample at different locations.

also improved because of the peening stresses that developed during grit blasting. Similarly, Rama Krishna et al.[26] also reported higher microhardness for FA coatings (430−470 $HV_{0.1}$) than the substrate (∼170 $HV_{0.1}$). This improvement was due to the presence of alumina (∼28%) in the FA. Also, Muhammad et al.[28] reported that higher microhardness (∼500 $HV_{0.1}$) was obtained for FA coatings (thickness <200 μm), and ascribed this to the large fraction of the fully molten region with less porosity (∼9.6%). However, the microhardness of the FA coating was lower because of the lower fraction of alumina and porous coatings.

Figure 6 elucidates the load versus depth curves for the FA coating and substrate. The elastic moduli of the coating and

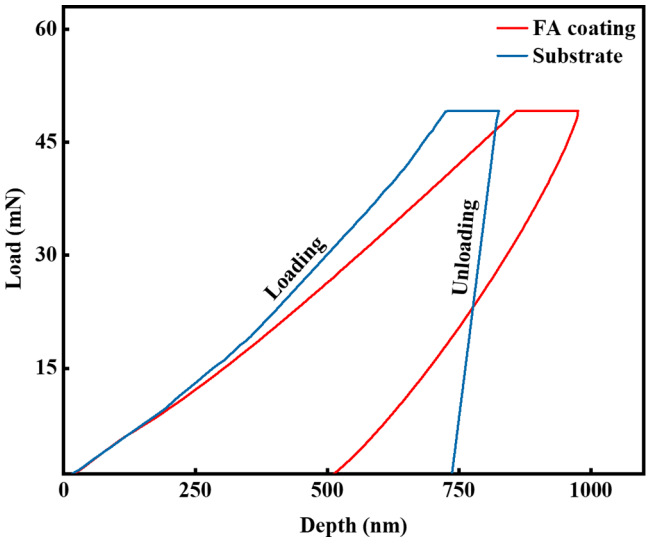

Figure 6. Load−depth curves of nanoindented FA coating and substrate.

substrate were 29.81 ± 3.48 and 200.16 ± 5.10 GPa, respectively. The higher porosity has reduced the elastic modulus and increased the penetration depth of the FA coating.

Figure 7 shows the indentation and induced cracks (C1 and C2) by the Vickers indenter. The fracture toughness of the FA coating was calculated using eq 4 as 0.43 ± 0.04 MPa$\sqrt{m}$ by considering the mean crack length. The lower fracture toughness of FA coating is attributed to the higher porosity. As a result of the pores, the crack propagates through the network of pores, and the fracture toughness is reduced.[51] Further addition of reinforcements/additives like alumina and CNT to the FA may enhance the fracture toughness.[52,53] The

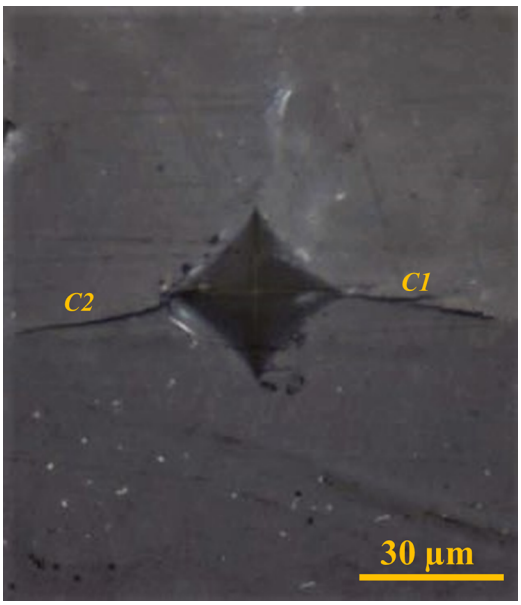

Figure 7. Indentation and induced cracks on an FA-coated sample.

results concerning such coatings are being investigated and will be communicated shortly.

Slurry Erosion Test Results. A slurry erosion test was performed to analyze the influence of the concentration of slurry, slurry rotational speed, and the impinging size of the particles on the erosive behavior of FA coatings developed on marine-grade steel. Weight loss for each experiment of FFD was noted, as listed in Table 4.

Effect of Mechanical Properties on Slurry Erosive Wear. The weight loss of uncoated substrate and FA coatings for different slurry concentrations, slurry rotating speeds, and sand particle sizes for a given test time of 3 h is shown in Table 4. Slurry erosive wear rate depends on the microhardness of the coating; hence, the FA-coated coupons showed much reduced erosive weight loss than the uncoated substrate. The higher hardness of the FA coating can withstand material loss when sand particles impact the surface of the coatings. It is worth noting that the hardness of the coating is not the only parameter that affects the wear rate, but also with lower hardness, some of the coatings have exhibited better wear resistance. For example, electroplated Ni−B coatings showed better wear resistance than hard Cr coatings because of their high hardness (H) to elastic modulus (E) ratio.[54] Table 3 shows that the H/E ratios of the FA coating and substrate were 0.1050 and 0.0075, respectively. These ratios indicate higher wear resistance of the coated specimen than the uncoated substrate, because coatings with high hardness and low elastic modulus are prone to have excellent wear resistance. Musil's group reported that radial cracks were absent in Al−Cu−O coatings whose H/E was >0.1.[55] However, radial cracks were observed in the FA coating because of its high porosity, resulting in lower fracture toughness. Figure 4b shows the detachment of coating from the substrate that was due to interlamellar cracks, which indicates poor bonding between interlayers of the FA coating. This poor bonding leads to severe wear when it is exposed to slurry erosive conditions. A few researchers have suggested using ceramic coatings to combat slurry erosion. Kumar Goyal et al.[56] found that high-velocity air fuel (HVAF)-sprayed WC-10Co-4Cr coating on steel exhibited more slurry erosion resistance than

https://doi.org/10.1021/acsomega.2c03800
ACS Omega 2022, 7, 32369−32382

Table 3. Mechanical Properties of the Coating and Substrate

	hardness (H) (GPa)	elastic modulus (E) (GPa)	H/E	fracture toughness (MPa$\sqrt{m}$)	coating adhesion strength (MPa)	porosity (%)
fly ash topcoat	3.13 ± 0.26	29.81 ± 3.48	0.1050	0.43 ± 0.04	5.62 ± 0.23	16−18
substrate	1.50 ± 0.14	200.16 ± 5.10	0.0075			

Al_2O_3+13TiO_2 coatings because of its improved hardness. Similarly, Grewal et al.[57] reported that erosion resistance was significantly affected by the proportion of alumina in the Ni−Al_2O_3-based composite coatings. The coating containing 40 wt % alumina exhibited the highest resistance among the coatings. This composite showed an ∼2.2 times lower erosion rate than uncoated steel. Also, Peat et al.[58] conducted slurry and dry jet erosion for high-velocity oxy-fuel (HVOF)-sprayed WC-CoCr, Cr_3C_2−NiCr, and Al_2O_3 coatings. The wear scar depth in WC-CoCr specimens decreased by ∼64%, indicating lower volume loss. The cobalt matrix's high coating hardness and capacity to hold the hard carbide particles were credited with lower volume loss with shallow wear scar depth. In the current investigation, FA coatings showed ∼11.11% better slurry erosive wear resistance than the uncoated specimen. Further, the slurry erosion resistance of the FA coatings could be improved with some additives like alumina and CNT.

Parts a and c of Figure 8 represent the 3D profiles of slurry erosion tested uncoated and FA-coated samples. More surface

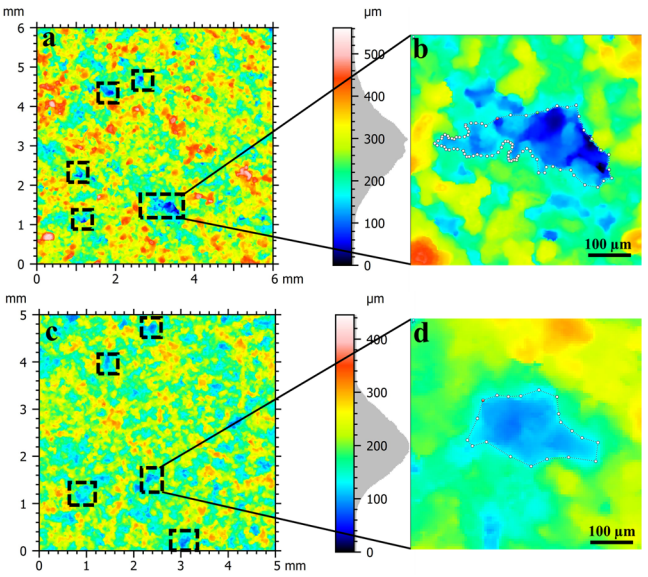

Figure 8. Three-dimensional surface profiles of slurry erosion tested samples: (a) uncoated, (c) FA-coated, and (b and d) the respective magnified profiles.

irregularities were observed in the uncoated substrate, which were due to scars that developed during the test, whereas FA coating limits the scar formation. Parts b and d of Figure 8 show more erodent penetration onto the uncoated substrate, resulting in more volume loss than that in the FA-coated sample. The quantification of volume loss of the FA-coated and uncoated samples was evaluated as 0.0007 ± 0.0001 and 0.0056 ± 0.0043 μm^3, respectively; the lower volume loss in the FA-coated sample is attributed to hard mullite phases.[59] Also, this was confirmed by the depth profiles of FA-coated and uncoated slurry erosion tested samples, as shown in Figure 9, parts a and b.

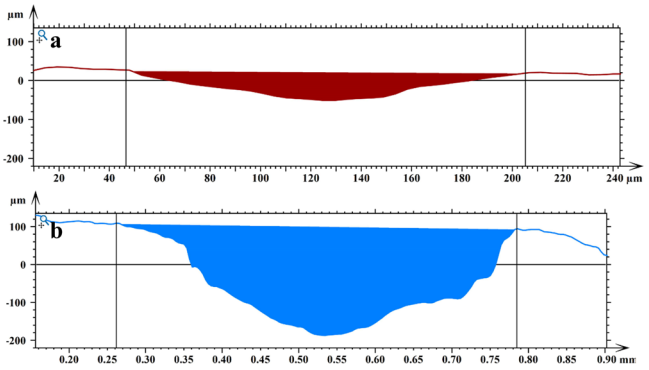

Figure 9. Depth profiles of slurry erosion tested samples: (a) FA-coated and (b) uncoated.

Effect of Slurry Erosion Process Parameters on Erosive Wear. Figure 10 represents the surface plots that provide the process parameters' combined effects on slurry erosive wear. The weight loss was increased with particle sizes from 210 to 300 μm (Figure 10a−d). Interestingly, a sharp decline in weight loss was reported corresponding to a particle size of 425 μm because the number of particles decreases for a given slurry concentration as particle size increases, resulting in fewer collisions of eroding particles during the slurry erosion study. Many researchers have suggested a power-law relationship between particle size and erosion rate.[60]

$$\text{erosion rate} = (\text{size of sand particle})^n$$

The value of n ranges from 0.3 to 2.0, depending on material properties, size, distribution of particles, and experimental conditions.[61]

Stack and Pungwiwat[62] claimed that no direct relation exists between erosion rate and particle size. They concluded that the different sizes of particles in a slurry have a complicated dynamic behavior that leads to the wear process in terms of particle shape, size, and impact velocity. According to Desale et al.,[63] the particle's lowest kinetic energy shifts the material's removal process from erosion to three-body abrasion. Smaller particles affect wear rate substantially more than larger particles during three-body abrasion. The weight loss has increased with slurry concentrations between 100 and 200 g/L. The penetration possibilities of slurry particles increase at lower slurry concentrations without much wear of slurry particles causing excessive erosion (Figure 11c), whereas at higher slurry concentrations, interparticle collisions can cause severe damage and fractures to the sand particles collected after the test, as shown in Figure 11b. These excessive damages and fractures result in a loss of surface strength and kinetic energy, resulting in decreased weight loss. Furthermore, large sand particles are broken down into smaller ones, resulting in a minor weight loss of 300 g/L. As the slurry rotation speed increases, more weight loss is observed in the case of both the uncoated and FA-coated coupons, which obey the Archards equation, $A = na^2\Pi$. In the present study, a and n represent the size and number of sand particles interacting with the sample

https://doi.org/10.1021/acsomega.2c03800
ACS Omega 2022, 7, 32369−32382

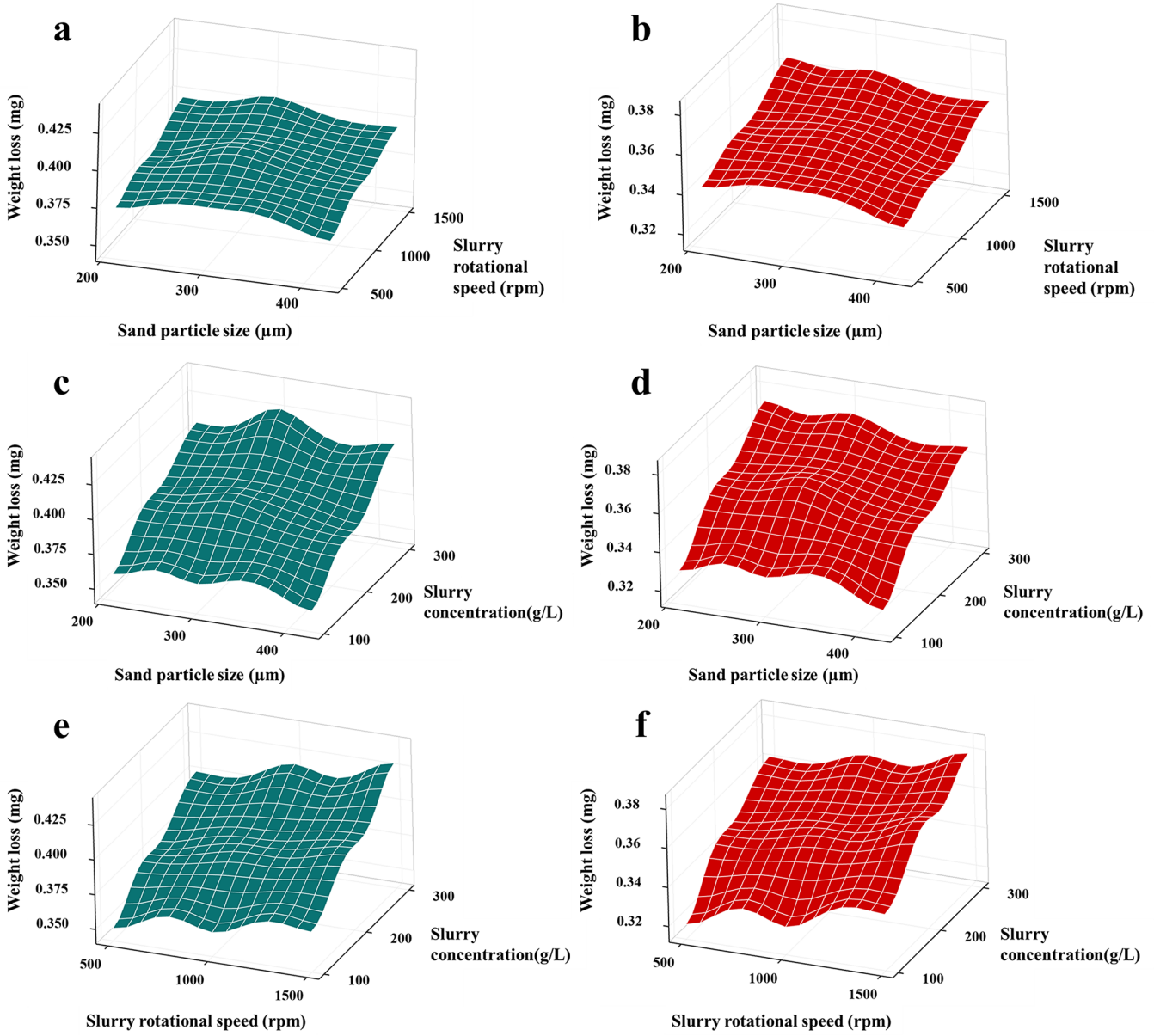

Figure 10. Interaction surface plots after the slurry erosion test: (a, c, and e) uncoated and (b, d, and f) FA-coated samples.

during the test (Π is a constant). The frequency of slurry contact on the target surface rises as the speed of slurry rotation for a given concentration of slurry increases, resulting in more weight loss. Bhandari et al.[64] made similar observations for the detonation gun sprayed Al_2O_3 and Al_2O_3−13 wt % TiO_2 ceramic coatings.

Full Factorial Analysis. The full factorial experimental design approach was used for experimentation, and the results are presented in Table 4. From Table 4, more weight loss occurred in the 18th run, and the parameters were a particle size of 300 μm, slurry rotational speed of 1500 rpm, and slurry concentration of 300 g/L. Similarly, minimum weight loss occurred in the 19th run, and the corresponding parameters were a particle size of 425 μm, slurry rotational speed of 500 rpm, and slurry concentration of 100 g/L.

Analysis of Variance. ANOVA was performed to find the critical parameters that affect the weight loss for uncoated and FA-coated samples. The *P*-values obtained by ANOVA are shown in Tables 5 and 6, indicating that all the factors significantly affect slurry erosive wear. The corresponding regression coefficients, R^2 and predicted R^2, for the uncoated substrate are 99.90% and 98.85%, and for FA-coated samples they are 99.95% and 99.44%, respectively.

Characterization of Slurry-Eroded Surfaces. The slurry erosion tested uncoated and FA-coated samples were taken for scanning electron microscopic imaging to analyze the wear mechanism. Figure 12 represents the scanning electron microscopy/energy-dispersive X-ray spectroscopy (SEM/EDS) images of slurry-eroded surfaces of uncoated and FA-coated samples. Figure 12a illustrates the presence of cracks, craters, plastic deformation of the surface, oxide layers, salt attack, corrosion pits, erosion pits, microchipping of material, spallation, and plowing of the material on the eroded surface of the uncoated sample. Cracks, plastic deformation, microchipping, erosion pits, and craters are due to the lower microhardness of the uncoated substrate. During the test, the sample was continuously exposed to a slurry of 3.5% NaCl, forming corrosion pits and deposition of salt onto the surface.

https://doi.org/10.1021/acsomega.2c03800
ACS Omega 2022, 7, 32369−32382

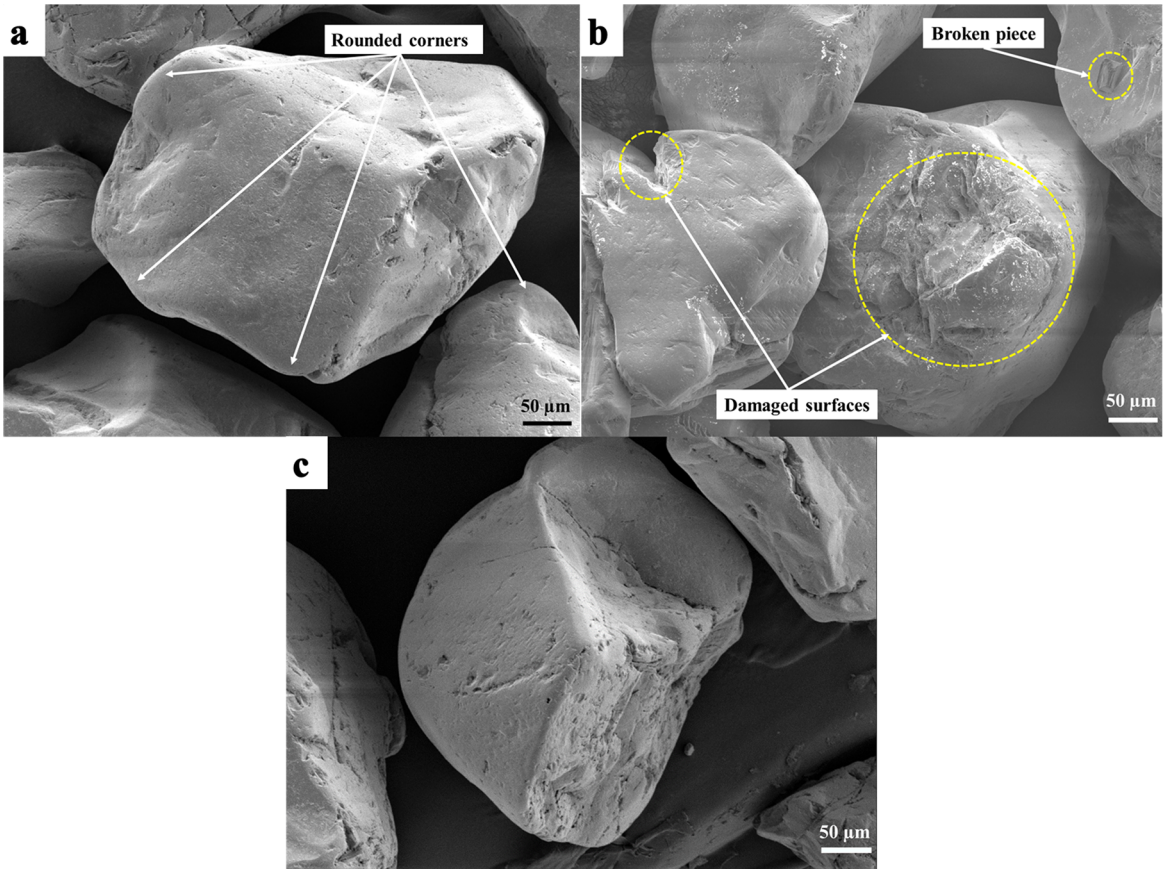

Figure 11. FESEM images of sand particles (a) before the test and (b and c) after the slurry erosion test at higher and lower slurry concentration, respectively.

In addition to erosion wear, corrosion pit formation damages the surfaces and accelerates the material removal rate. The FA coating was deposited onto the substrate to enhance the wear resistance. Figure 12b shows the eroded surface of the FA-coated sample after the slurry erosion test. The presence of cracks, spallation, corrosion pits, and surface plastic deformation is minimal because of the protective coating. However, the material was removed by spallation because of poor cohesive bonding of the top layers in the coating and high porosity. Even though the sample was exposed to 3.5% NaCl during the test, corrosion pits and salt formation on the surface were minimal because the FA-coated sample has a glassy quartz phase that resists the corrosion. However, because of the porosity of the FA coating, some corrosion pits were observed on the surface. Figure 12c depicts the EDS of the uncoated slurry erosion tested sample; it is evident that an iron composition of 73.74 wt % was observed because of its exposure to a saline environment during the test, which induces more corrosion products. In contrast, from Figure 12d, 25.94 wt % of iron was retained along with aluminum and silicon peaks, which were the predominant constituents of the FA. This retainment proves the sustainability of the FA coating after the test.

Corrosion Results. *Salt Spray Test Analysis.* Figure 14 depicts the corrosion rate of both FA-coated and uncoated substrates. The study shows the material degradation over the period. After being exposed to salt fog for a specific time, red rust formation was observed in uncoated and FA-coated samples. The emergence of red rust was detected at the early stage (at the end of 24 h) on the uncoated marine-grade steel samples, as shown in Figure 13a. Significant formation of red rust was observed in the FA-coated pieces after 48 h; see Figure 13b. The weight loss of uncoated and coated substrates increases dramatically as the exposure period increases. The uncoated model loses much more weight than the coated sample after 168 h. The corrosion rate, calculated in terms of the weight loss of uncoated and coated samples, was 263.04 ± 2.91 and 227.55 ± 2.83 μm/year, respectively. The average corrosion rate of the FA coating was improved by ∼13.49% compared to that of the uncoated substrate. The FA coating surfaces have more resistance to chemical attack because of the glassy quartz and corrosion stability that is due to the mullite phase.[47] As a result, the coatings exhibit superior corrosion resistance for a prolonged duration. Porosity was observed in the coating, which allows the molten salt to penetrate and leads to corrosion. Coating flaws and the impurities on the surface lead to the formation of pitting corrosion.[65,66] Sreenivas Rao et al.[67] reported a similar observation for plasma-sprayed Cr_2O_3−Al_2O_3−ZrO_2 multilayer coatings on mild steel. However, depositing dense FA coatings can further improve the corrosion resistance.

Electrochemical Impedance Spectroscopy Analysis. Figure 15a shows the polarization curves for uncoated and FA-coated substrates. The I_{corr}, E_{corr} values corresponding to uncoated and coated samples, calculated using Tafel plot extrapolation, were 1.0149×10^{-4} mA/cm^2, −672.7425 mV and 0.2336×10^{-4} mA/cm^2, −695.3294 mV, respectively. During the polarization test, the potential was increased at a rate of 5 mV, and a significant decline in corrosion current occurred, followed by an anodic current near the corrosion potential. The potential

https://doi.org/10.1021/acsomega.2c03800
ACS Omega 2022, 7, 32369−32382

Table 4. Experimental Plan and Corresponding Results as per Full Factorial Design

Sl. no.	particle size (μm)	slurry speed (rpm)	slurry concentration (g/L)	av weight loss of uncoated sample (mg)	av weight loss of coated sample (mg)
1	210	500	100	0.3493	0.3191
2	210	500	200	0.3760	0.3452
3	210	500	300	0.3952	0.3628
4	210	1000	100	0.3552	0.3263
5	210	1000	200	0.3851	0.3533
6	210	1000	300	0.4063	0.3740
7	210	1500	100	0.3710	0.3421
8	210	1500	200	0.3993	0.3677
9	210	1500	300	0.4200	0.3835
10	300	500	100	0.3514	0.3233
11	300	500	200	0.3823	0.3543
12	300	500	300	0.4111	0.3664
13	300	1000	100	0.3621	0.3311
14	300	1000	200	0.3982	0.3622
15	300	1000	300	0.4293	0.3741
16	300	1500	100	0.3693	0.3430
17	300	1500	200	0.4063	0.3701
18	300	1500	300	0.4393	0.3810
19	425	500	100	0.3452	0.3160
20	425	500	200	0.3683	0.3412
21	425	500	300	0.3967	0.3573
22	425	1000	100	0.3533	0.3213
23	425	1000	200	0.3842	0.3490
24	425	1000	300	0.4172	0.3644
25	425	1500	100	0.3653	0.3373
26	425	1500	200	0.3916	0.3623
27	425	1500	300	0.4292	0.3753

Table 5. Uncoated Substrate ANOVA Results

sources	adj SS[a]	*P*-value
sand particle size	0.000673	0.000
slurry rotational speed	0.002591	0.000
slurry concentration	0.015151	0.000
sand particle size × slurry rotational speed	0.000048	0.026
sand particle size × slurry concentration	0.000276	0.000
slurry rotational speed × slurry concentration	0.000076	0.007
error	0.000019	
total	0.018833	

[a]adj SS: adjusted sum of squares.

Table 6. FA Coating ANOVA Results

sources	adj SS[a]	*P*-value
sand particle size	0.000374	0.000
slurry rotational speed	0.001761	0.000
slurry concentration	0.008225	0.000
sand particle size × slurry rotational speed	0.000030	0.002
sand particle size × slurry concentration	0.000037	0.001
slurry rotational speed × slurry concentration	0.000023	0.005
error	0.000005	
total	0.010455	

[a]adj SS: adjusted sum of squares.

corresponding to an abrupt corrosion current reduction is called the pitting potential ($E_{pitting}$); localized corrosion and hydrogen evolution occur at this potential. The shift in the polarization graph toward the left for the FA coating indicates the low corrosion current density compared to that of the uncoated substrate, which further decreases the corrosion rate of the FA coating. Husain et al.[68] reported similar observations for h-BN-based spin coatings. Abdollahi et al.[69] reported a similar shift in the polarization plot for sol−gel-processed alkoxysilane compared to bare aluminum. Manivannan et al.[70] made similar observations for calcium-doped AZ61 alloy under similar testing conditions. Figure 15b represents impedance data of uncoated and FA-coated substrates. It shows that the FA-coated substrate has a higher impedance because of the formation of a passive film which further enhances the corrosion resistance of the FA coating compared to that of the uncoated substrate. This study indicates that the FA coating on the substrate is an effective barrier that prevents chlorine ions from penetrating the substrate and improves corrosion resistance. The Nyquist plot is presented in Figure 15c. The large diameter curve in the Nyquist plot for the FA-coated substrate reveals a higher actual impedance (Z''), indicating higher capacitance, and hence it offers better corrosion protection. Similar observations were made by Husain et al.[68] for conventional h-BN spin-coated coupons under simulated seawater media.

CONCLUSIONS

Atmospheric plasma-sprayed FA coatings with a thickness 291.72 ± 26.89 μm and porosity of 16−18% were successfully deposited on marine-grade steel without delamination. The following conclusions are drawn from the results embodied in the investigation:

1. The mechanical properties of the FA coatings, such as microhardness, adhesion strength, and fracture toughness, were evaluated. The mineralogy of FA enhances the microhardness of the coatings by ∼109.48% compared to that of an uncoated substrate. The

https://doi.org/10.1021/acsomega.2c03800
ACS Omega 2022, 7, 32369−32382

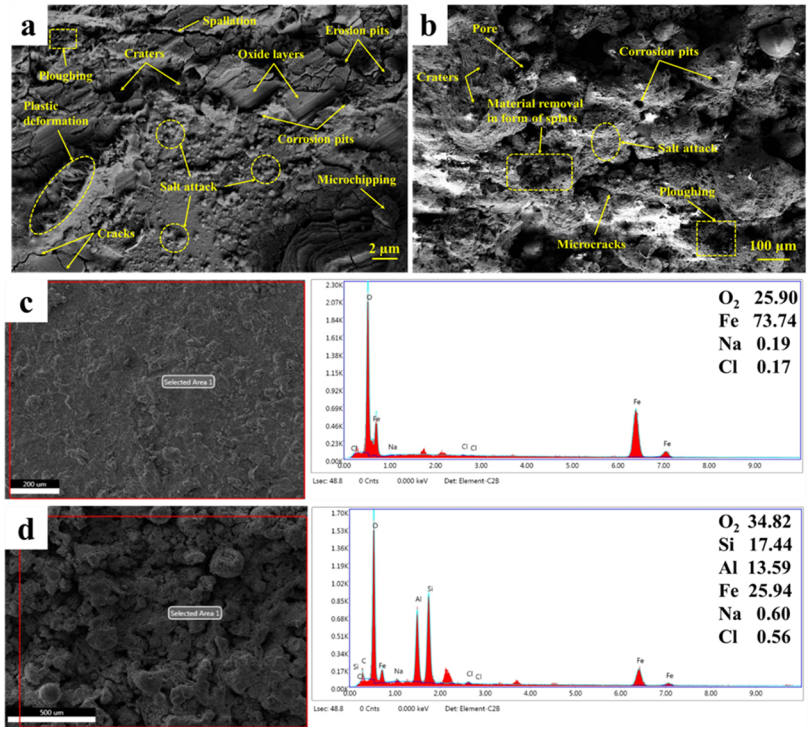

Figure 12. Scanning electron microscopic images of slurry-eroded surfaces: (a) uncoated and (b) FA-coated substrates. EDS on the tested samples: (c) uncoated and (d) FA-coated.

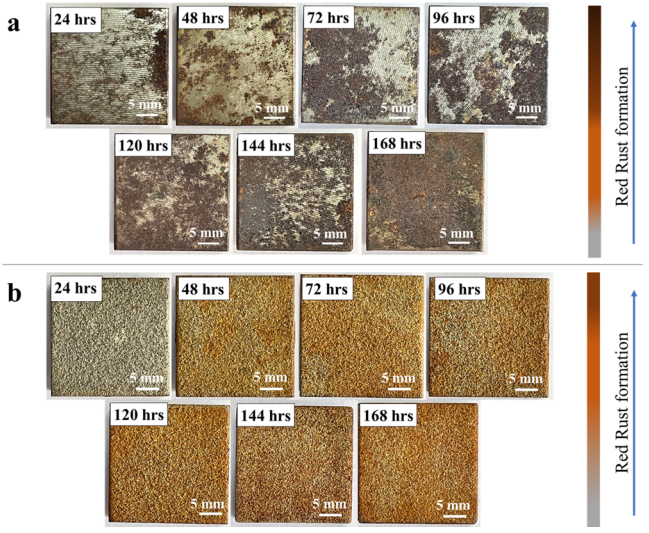

Figure 13. Digital imaging of salt spray tested samples: (a) uncoated; (b) FA-coated.

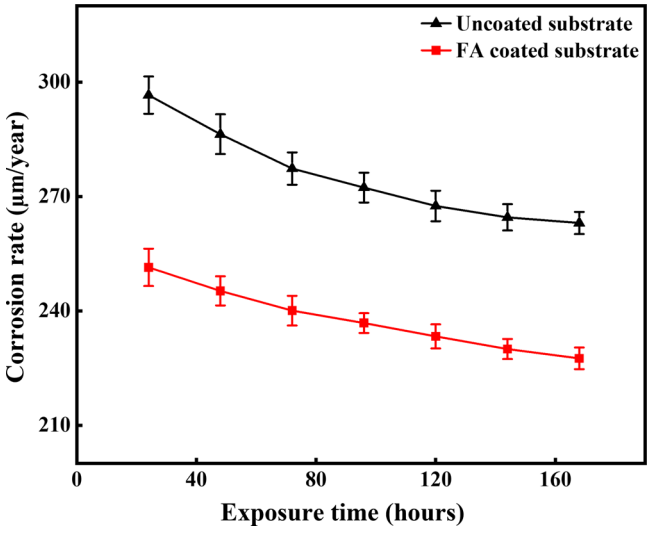

Figure 14. Corrosion rate of uncoated and FA-coated substrates at different exposure times.

adhesion strength (5.62 ± 0.23 MPa) and fracture toughness (0.43 ± 0.04 MPa$\sqrt{m}$) were observed to be less because of the high porosity of the coating.

2. Although the H/E ratio of the FA coating was significantly higher, the slurry erosion wear resistance was improved by only ∼11.11% because of low fracture toughness.
3. As confirmed by ANOVA, slurry concentration and rotational speeds were the dominant factors influencing slurry erosion wear for uncoated substrates and FA coatings. The slurry erosion wear mechanism was studied using FESEM images, which revealed that the surface's damage was significantly less for FA coatings than uncoated substrate because of its unique mineralogy.
4. The corrosion resistance of the FA coating was enhanced by ∼13.49% compared to the uncoated substrate in the salt spray test. EIS analysis was used to study the electrochemical aspects of the corrosion. The I_{corr}, E_{corr} values corresponding to uncoated and coated samples, calculated using Tafel plot extrapolation, were 1.0149×10^{-4} mA/cm^2, −672.7425 mV and 0.2336×10^{-4} mA/cm^2, −695.3294 mV, respectively.

The authors believe that specific additives, like alumina and CNT, can be used to further improve the FA coating's slurry erosion wear and corrosion resistance, because of the

https://doi.org/10.1021/acsomega.2c03800
ACS Omega 2022, 7, 32369−32382

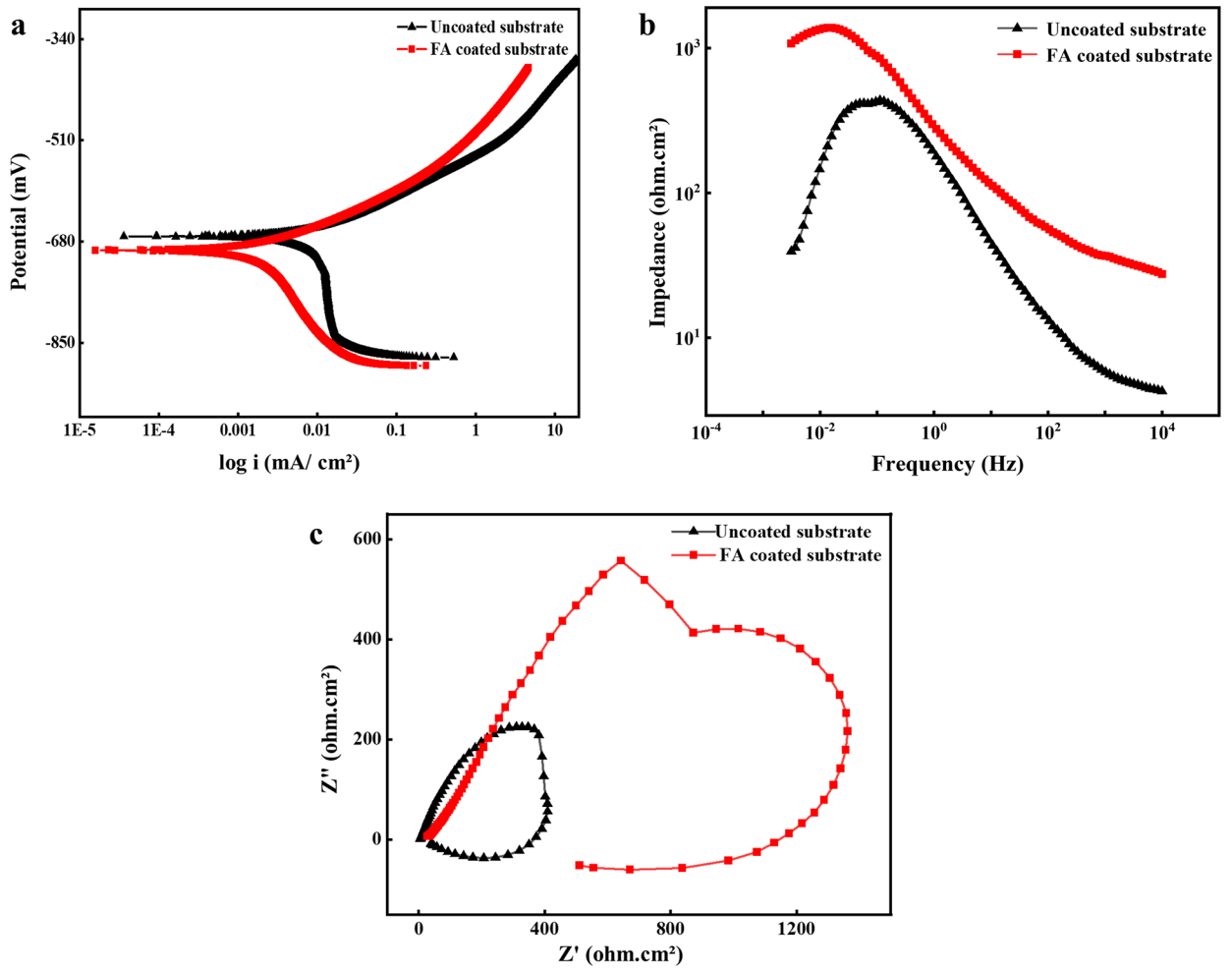

Figure 15. EIS plots of uncoated and FA-coated substrates: (a) polarization curves, (b) impedance, and (c) Nyquist plots.

densification of the coating. Such doped FA coatings can find potential applications in marine and offshore parts like ship hull structures and ballast tanks to enhance erosion and corrosion resistance.

AUTHOR INFORMATION

Corresponding Author

Sudhakar C. Jambagi − *Department of Mechanical Engineering, National Institute of Technology Karnataka, 575025 Surathkal, India;* orcid.org/0000-0001-7236-5090; Email: sudhakar@nitk.edu.in

Authors

Nagarjuna Chavana − *Department of Mechanical Engineering, National Institute of Technology Karnataka, 575025 Surathkal, India;* orcid.org/0000-0002-9402-4868

Vishwanath Bhajantri F − *Department of Mechanical Engineering, National Institute of Technology Karnataka, 575025 Surathkal, India;* orcid.org/0000-0002-3663-7789

Complete contact information is available at: https://pubs.acs.org/10.1021/acsomega.2c03800

Author Contributions

N.C. and V.B.F. contributed equally to this work. The manuscript was written with the contributions of all authors. All have approved the final version of the manuscript.

Notes

The authors declare no competing financial interest.

ACKNOWLEDGMENTS

The authors would like to express their sincere thanks to the Department of Mechanical Engineering and the Central Research Facility (CRF), the National Institute of Technology, Karnataka, for providing access to the electrochemical impedance spectroscopy, field emission scanning electron microscopy, X-ray diffraction, and 3D profilometer facilities.

REFERENCES

(1) *Report on Fly Ash Generation at Coal/Lignite Based Thermal Power Stations and Its Utilization in the Country for the Year 2020−21*; Central Electricity Authority Thermal Civil Design Division: New Delhi, India, 2021.

(2) Yao, Z. T.; Ji, X. S.; Sarker, P. K.; Tang, J. H.; Ge, L. Q.; Xia, M. S.; Xi, Y. Q. A Comprehensive Review on the Applications of Coal Fly Ash. *Earth-Science Rev.* **2015**, *141*, 105−121.

(3) Skodras, G.; Grammelis, P.; Kakaras, E.; Karangelos, D.; Anagnostakis, M.; Hinis, E. Quality Characteristics of Greek Fly Ashes and Potential Uses. Fuel Process. Technol. *Fuel Process. Technol.* **2007**, *88*, 77−85.

(4) Belviso, C. State-of-the-Art Applications of Fly Ash from Coal and Biomass: A Focus on Zeolite Synthesis Processes and Issues. *Prog. Energy Combust. Sci.* **2018**, *65*, 109−135.

(5) Eliche-Quesada, D.; Sandalio-Pérez, J. A.; Martínez-Martínez, S.; Pérez-Villarejo, L.; Sánchez-Soto, P. J. Investigation of Use of Coal Fly

https://doi.org/10.1021/acsomega.2c03800
ACS Omega 2022, 7, 32369−32382

Ash in Eco-Friendly Construction Materials: Fired Clay Bricks and Silica-Calcareous Non Fired Bricks. *Ceram. Int.* **2018**, *44*, 4400−4412.
(6) Erol, M.; Küçükbayrak, S. E.-M. A.; Ersoy-Meriçboyu, A. Comparison of the Properties of Glass, Glass−Ceramic and Ceramic Materials Produced from Coal Fly Ash. *J. Hazard. Mater.* **2008**, *153*, 418−425.
(7) Kikuchi, R. Application of Coal Ash to Environmental Improvement: Transformation into Zeolite, Potassium Fertilizer, and FGD Absorbent. *Resour. Conserv. Recycl.* **1999**, *27*, 333−346.
(8) Iyer, R. S.; Scott, J. A. Power Station Fly Ash - A Review of Value-Added Utilization Outside of the Construction Industry. *Resour. Conserv. Recycl.* **2001**, *31*, 217−228.
(9) Wang, L.; Zhang, Y.; Chen, L.; Guo, B.; Tan, Y.; Sasaki, K.; Tsang, D. C. W. Designing Novel Magnesium Oxysulfate Cement for Stabilization/Solidification of Municipal Solid Waste Incineration Fly Ash. *J. Hazard. Mater.* **2022**, *423*, 127025.
(10) Chen, L.; Wang, L.; Zhang, Y.; Ruan, S.; Mechtcherine, V.; Tsang, D. C. W. Roles of Biochar in Cement-Based Stabilization/Solidification of Municipal Solid Waste Incineration Fly Ash. *Chem. Eng. J.* **2022**, *430*, 132972.
(11) Bieliatynskyi, A.; Yang, S.; Pershakov, V.; Shao, M.; Ta, M. The Use of Fiber Made from Fly Ash from Power Plants in China in Road and Airfield Construction. *Constr. Build. Mater.* **2022**, *323*, 126537.
(12) Rayalu, S.; Meshram, S. U.; Hasan, M. Z. Highly Crystalline Faujasitic Zeolites from Flyash. *J. Hazard. Mater.* **2000**, *77*, 123−131.
(13) Tanaka, H.; Sakai, Y.; Hino, R. Formation of Na-A and -X Zeolites from Waste Solutions in Conversion of Coal Fly Ash to Zeolites. *Mater. Res. Bull.* **2002**, *37*, 1873−1884.
(14) Querol, X.; Moreno, N.; Umaña, J. C.; Alastuey, A.; Hernández, E.; López-Soler, A.; Plana, F. Synthesis of Zeolites from Coal Fly Ash: An Overview. *Int. J. Coal Geol.* **2002**, *50*, 413−423.
(15) Ahmaruzzaman, M. A Review on the Utilization of Fly Ash. *Prog. Energy Combust. Sci.* **2010**, *36*, 327−363.
(16) Bukhari, S. S.; Behin, J.; Kazemian, H.; Rohani, S. Conversion of Coal Fly Ash to Zeolite Utilizing Microwave and Ultrasound Energies: A Review. *Fuel* **2015**, *140*, 250−266.
(17) Koshy, N.; Singh, D. N. Fly Ash Zeolites for Water Treatment Applications. *J. Environ. Chem. Eng.* **2016**, *4*, 1460−1472.
(18) Chauhan, S. R.; Thakur, S. Effects of Particle Size, Particle Loading and Sliding Distance on the Friction and Wear Properties of Cenosphere Particulate Filled Vinylester Composites. *Mater. Des.* **2013**, *51*, 398−408.
(19) Siddique, R. Utilization of Coal Combustion By-Products in Sustainable Construction. *Resour. Conserv. Recycl.* **2010**, *54*, 1060−1066.
(20) *Annual Book of ASTM Standards: Standard Specification for Coal Fly Ash and Raw or Calcined Natural Pozzolan for Use in Concrete*; ASTM C618-17a; ASTM International: West Conshohocken, PA, 2017; pp 1−5.
(21) Bhajantri, V.; Krishna, P.; Jambagi, S. A Brief Review on Fly Ash and Its Use in Surface Engineering. *AIP Conf. Proc.* **2018**, *1943*, 020028.
(22) Pawlowski, L. *The Science and Engineering of Thermal Spray Coatings*, 2nd ed.; John Wiley & Sons Ltd.: Chichester, U.K., 2008.
(23) Khor, K. A.; Gu, Y. W. Thermal Properties of Plasma-Sprayed Functionally Graded Thermal Barrier Coatings. *Thin Solid Films* **2000**, *372*, 104−113.
(24) Çelik, E.; Şengil, I. A.; Avci, E. Effects of Some Parameters on Corrosion Behaviour of Plasma-Sprayed Coatings. *Surf. Coat. Technol.* **1997**, *97*, 355−360.
(25) Celik, E.; Ozdemir, I.; Avci, E.; Tsunekawa, Y. Corrosion Behaviour of Plasma Sprayed Coatings. *Surf. Coat. Technol.* **2005**, *193*, 297−302.
(26) Rama Krishna, L.; Sen, D.; Srinivasa Rao, D.; Sundararajan, G. Coatability and Characterization of Fly Ash Deposited on Mild Steel by Detonation Spraying. *J. Therm. Spray Technol* **2003**, *12*, 77−79.
(27) Sidhu, B. S.; Singh, H.; Puri, D.; Prakash, S. Wear and Oxidation Behaviour of Shrouded Plasma Sprayed Fly Ash Coatings. *Tribol. Int.* **2007**, *40*, 800−808.
(28) Muhammad, M. M.; Isa, M. C.; Shamsudin, R.; Jalar, A. Plasma Spray Deposition of Fly Ash onto Mild Steel Substrates Using a Fractional Factorial Design Approach. *Ceram. Int.* **2014**, *40*, 13635−13642.
(29) Ulutan, M.; Kılıçay, K.; Kaya, E.; Bayar, İ Plasma Transferred Arc Surface Modification of Atmospheric Plasma Sprayed Ceramic Coatings. *J. Mech. Sci. Technol.* **2016**, *30*, 3813−3818.
(30) Kılıçay, K.; Kaya, E. Improvement of Microstructural and Tribological Properties of APS Carbide Coatings via PTA Surface Melting. *Trans. Inst. Met. Finish.* **2020**, *98*, 129−137.
(31) Naveena, B. E.; Keshavamurthy, R.; Sekhar, N. Slurry Erosive Wear Behaviour of Plasma-Sprayed Flyash−Al_2O_3 Coatings. *Surf. Eng.* **2017**, *33*, 925−935.
(32) Keshavamurthy, R.; Naveena, B. E.; Ahamed, A.; Sekhar, N.; Peer, D. Corrosion Characteristics of Plasma Sprayed Flyash-SiC and Flyash-Al_2O_3 Composite Coatings on the Al-6061 Alloy. *Mater. Res. Express* **2019**, *6*, 0865i4.
(33) Mishra, S. C.; Satpathy, A.; Singh, K. P.; Padmanabham, P. V. A. Plasma Spray Coating of Fly Ash on Metals for Tribological Application. In *Proceedings of the International Seminar on Mineral Processing Technology*, Chennai, India; Khosia, N. K., Jadhav, G. N., Eds.; Indian Institute of Technology, Indian Institute of Mineral Engineers (India), Ashapura Group: Mumbai, India, 2006; pp 825−829.
(34) Yin, Z.; Tao, S.; Zhou, X.; Ding, C. Particle In-Flight Behavior and Its Influence on the Microstructure and Mechanical Properties of Plasma-Sprayed Al_2O_3 Coatings. *J. Eur. Ceram. Soc.* **2008**, *28*, 1143−1148.
(35) *ASTM Special Technical Publications: Standard Practice for Preparing, Cleaning and Evaluating Corrosion Test Specimens*; ASTM G1-03; ASTM International: West Conshohocken, PA, 1985; pp 505−510.
(36) *Standard Test Method for Adhesion or Cohesion Strength of Thermal Spray Coatings*; ASTM C633-13; ASTM International: West Conshohocken, PA, 2017.
(37) Oliver, W. C.; Pharr, G. M. An Improved Technique for Determining Hardness and Elastic Modulus Using Load and Displacement Sensing Indentation Experiments. *J. Mater. Res.* **1992**, *7*, 1564−1583.
(38) Anstis, G. R.; ChantikuL, P.; Lawn, B. R.; Marshall, D. B. A Critical Evaluation of Indentation Techniques for Measuring Fracture Toughness: I, Direct Crack Measurements. *J. Am. Ceram. Soc.* **1981**, *64*, 533−538.
(39) Zamani, P.; Valefi, Z. Microstructure, Phase Composition and Mechanical Properties of Plasma Sprayed Al_2O_3, Cr_2O_3 and Cr_2O_3-Al_2O_3 Composite Coatings. *Surf. Coat. Technol.* **2017**, *316*, 138−145.
(40) *Standard Practice for Operating Salt Spray (FOG) Apparatus*; ASTM B117-18; ASTM International: West Conshohocken, PA, 2003; pp 1−15.
(41) *ASTM Special Technical Publications: Standard Practice For Laboratory Immersion Corrosion Testing of Metals*; ASTM G31-72; ASTM International: West Conshohocken, PA, 1985; pp 534−544.
(42) Zhao, Y.; Cui, Y.; Hasebe, Y.; Bian, H.; Yamanaka, K.; Aoyagi, K.; Hagisawa, T.; Chiba, A. Controlling Factors Determining Flowability of Powders for Additive Manufacturing: A Combined Experimental and Simulation Study. *Powder Technol.* **2021**, *393*, 482−493.
(43) Reed, R. *The Superalloys: Fundamentals and Applications*; Cambridge University Press: Cambridge, U.K., 2008.
(44) Bose, S. High-Temperature Corrosion. *High-Temperature Coatings*; Elsevier: Burlington, MA, 2017; pp 53−70.
(45) Park, Y. M.; Yang, T. Y.; Yoon, S. Y.; Stevens, R.; Park, H. C. Mullite Whiskers Derived from Coal Fly Ash. *Mater. Sci. Eng., A* **2007**, *454*−*455*, 518−522.
(46) Schneider, H.; Schreuer, J.; Hildmann, B. Structure and Properties of Mullite-A Review. *J. Eur. Ceram. Soc.* **2008**, *28*, 329−344.

https://doi.org/10.1021/acsomega.2c03800
ACS Omega 2022, 7, 32369−32382

(47) Okamoto, Y.; Fukudome, H.; Hayashi, K.; Nishikawa, T. Creep Deformation of Polycrystalline Mullite. *J. Eur. Ceram. Soc.* **1990**, *6*, 161−168.
(48) Kollenberg, W.; Schneider, H. Microhardness of Mullite at Temperatures to 1000°. *J. Am. Ceram. Soc.* **1989**, *72*, 1739−1740.
(49) Ghasemi, R.; Vakilifard, H. Plasma-Sprayed Nanostructured YSZ Thermal Barrier Coatings: Thermal Insulation Capability and Adhesion Strength. *Ceram. Int.* **2017**, *43*, 8556−8563.
(50) Yilmaz, Ş. An Evaluation of Plasma-Sprayed Coatings Based on Al_2O_3 and Al_2O_3−13 Wt.% TiO_2 with Bond Coat on Pure Titanium Substrate. *Ceram. Int.* **2009**, *35*, 2017−2022.
(51) Thakare, J. G.; Pandey, C.; Mulik, R. S.; Mahapatra, M. M. Mechanical Property Evaluation of Carbon Nanotubes Reinforced Plasma Sprayed YSZ-Alumina Composite Coating. *Ceram. Int.* **2018**, *44*, 6980−6989.
(52) Jambagi, S. C.; Kar, S.; Brodard, P.; Bandyopadhyay, P. P. Characteristics of Plasma Sprayed Coatings Produced from Carbon Nanotube Doped Ceramic Powder Feedstock. *Mater. Des* **2016**, *112*, 392−401.
(53) Jambagi, S. C.; Sarkar, N.; Bandyopadhyay, P. P. Preparation of Carbon Nanotube Doped Ceramic Powders for Plasma Sprayingusing Heterocoagulation Method. *J. Eur. Ceram. Soc.* **2015**, *35*, 989−1000.
(54) Liang, Y.; Li, Y. S.; Yu, Q. Y.; Zhang, Y. X.; Zhao, W. j.; Zeng, Z. X. Structure and Wear Resistance of High Hardness Ni-B Coatings as Alternative for Cr Coatings. *Surf. Coat. Technol.* **2015**, *264*, 80−86.
(55) Blažek, J.; Musil, J.; Stupka, P.; Čerstvý, R.; Houška, J. Properties of Nanocrystalline Al-Cu-O Films Reactively Sputtered by DC Pulse Dual Magnetron. *Appl. Surf. Sci.* **2011**, *258*, 1762−1767.
(56) Kumar Goyal, D.; Singh, H.; Kumar, H.; Sahni, V. Slurry Erosion Behaviour of HVOF Sprayed WC−10Co−4Cr and Al_2O_3+13TiO_2 Coatings on a Turbine Steel. *Wear* **2012**, *289*, 46−57.
(57) Grewal, H. S.; Arora, H. S.; Agrawal, A.; Singh, H.; Mukherjee, S. Slurry Erosion of Thermal Spray Coatings: Effect of Sand Concentration. *Procedia Eng.* **2013**, *68*, 484−490.
(58) Peat, T.; Galloway, A.; Toumpis, A.; Harvey, D.; Yang, W. H. Performance Evaluation of HVOF Deposited Cermet Coatings under Dry and Slurry Erosion. *Surf. Coat. Technol.* **2016**, *300*, 118−127.
(59) Ananthakumar, S.; Jayasankar, M.; Warrier, K. G. K. Microstructural, Mechanical and Thermal Characterization of Sol−Gel-Derived Aluminium Titanate−Mullite Ceramic Composites. *Acta Mater.* **2006**, *54*, 2965−2973.
(60) Ojala, N.; Valtonen, K.; Kivikytö-Reponen, P.; Vuorinen, P.; Siitonen, P.; Kuokkala, V.-T. Effect of Test Parameters on Large Particle High Speed Slurry Erosion Testing. *Tribol. - Mater. Surf. Interfaces* **2014**, *8*, 98−104.
(61) Gandhi, B. K.; Borse, S. V. Nominal Particle Size of Multi-Sized Particulate Slurries for Evaluation of Erosion Wear and Effect of Fine Particles. *Wear* **2004**, *257*, 73−79.
(62) Stack, M. M.; Pungwiwat, N. Slurry Erosion of Metallics, Polymers, and Ceramics: Particle Size Effects. *Mater. Sci. Technol.* **1999**, *15*, 337−344.
(63) Desale, G. R.; Gandhi, B. K.; Jain, S. C. Particle Size Effects on the Slurry Erosion of Aluminium Alloy (AA 6063). *Wear* **2009**, *266*, 1066−1071.
(64) Bhandari, S.; Singh, H. K.; Kansal, K.; Rastogi, V. Slurry Erosion Behaviour of Detonation Gun Spray Al_2O_3 and Al_2O_3-13TiO_2- Coated CF8M Steel Under Hydro Accelerated Conditions. *Tribol. Lett.* **2012**, *45*, 319−331.
(65) Malik, V. R.; Bajakke, P. A.; Jambagi, S. C.; Nagarjuna, C.; Deshpande, A. S. Investigating Mechanical and Corrosion Behavior of Plain and Reinforced AA1050 Sheets Fabricated by Friction Stir Processing. *JOM* **2020**, *72*, 3582−3593.
(66) Bajakke, P. A.; Jambagi, S. C.; Malik, V. R.; Deshpande, A. S. Friction Stir Processing: An Emerging Surface Engineering Technique. In *Surface Engineering of Modern Materials*; Gupta, K., Ed.; Springer: Cham, Switzerland, 2020; pp 1−31.
(67) Sreenivas Rao, K. V.; Tejaswini, G. C.; Girisha, K. G. Corrosion Behavior of Plasma Sprayed Cr_2O_3 - Al_2O_3 - ZrO_2 Multilayer Coatings on Mild Steel. Mater. *Mater. Today: Proc.* **2018**, *5*, 24068−24074.
(68) Husain, E.; Narayanan, T. N.; Taha-Tijerina, J. J.; Vinod, S.; Vajtai, R.; Ajayan, P. M. Marine Corrosion Protective Coatings of Hexagonal Boron Nitride Thin Films on Stainless Steel. *ACS Appl. Mater. Interfaces* **2013**, *5*, 4129−4135.
(69) Abdollahi, H.; Ershad-Langroudi, A.; Salimi, A.; Rahimi, A. Anticorrosive Coatings Prepared Using Epoxy-Silica Hybrid Nanocomposite Materials. *Ind. Eng. Chem. Res.* **2014**, *53*, 10858−10869.
(70) Manivannan, S.; Dinesh, P.; Babu, S. P. K.; Sundarrajan, S. Investigation and Corrosion Performance of Cast Mg-6Al-1Zn + XCa Alloy under Salt Spray Test (ASTM-B117). *J. Magnesium Alloys* **2015**, *3*, 86−94.

https://doi.org/10.1021/acsomega.2c03800
ACS Omega 2022, 7, 32369−32382